BIOCHEMISTRY

ATG16L1 adopts a dual–binding site mode to interact with WIPI2b in autophagy

Xinyu Gong[1], Yingli Wang[1], Yubin Tang[1], Yaru Wang[1], Mingfang Zhang[1], Miao Li[2], Yuchao Zhang[1], Lifeng Pan[1,2]*

Macroautophagy plays crucial roles in the regulation of cellular physiology and requires de novo synthesis of double-membrane autophagosomes, which relies on a specific interaction between autophagy-related 16L1 (ATG16L1) and WD repeat domain phosphoinositide-interacting protein 2b (WIPI2b). However, the molecular mechanism governing the interaction of ATG16L1 with WIPI2b remains elusive. Here, we find that ATG16L1 has two distinct binding sites for interacting with WIPI2b, the previously reported WIPI2b-binding site (WBS1) and the previously unidentified site (WBS2). We determine the crystal structures of WIPI2b with ATG16L1 WBS1 and WBS2, respectively, and elucidate the molecular mechanism underpinning the recruitment of ATG16L1 by WIPI2b. Moreover, we uncover that ATG16L1 WBS2 and its binding mode with WIPI2b is well conserved from yeast to mammals, unlike ATG16L1 WBS1. Last, our cell-based functional assays demonstrate that both ATG16L1 WBS1 and WBS2 are required for the effective autophagic flux. In conclusion, our findings provide mechanistic insights into the key ATG16L1/WIPI2b interaction in autophagy.

INTRODUCTION

Macroautophagy (hereafter referred to as autophagy) is a well conserved and regulated catabolic process involving lysosome-dependent degradation of undesired or harmful cytosolic components, such as bulk protein aggregates, dysfunctional organelles, and invasive pathogens, for maintaining cellular homeostasis and physiology in mammals (*1*–*5*). During autophagy, the encapsulation of autophagic cargoes for delivery to lysosomes relies on the unique double-membraned vesicles termed as autophagosomes, which are generated through several sequential steps mediated by the coordinated actions of a series of core autophagic proteins (*4*–*10*). In particular, in nonselective canonical autophagy, such as the starvation-induced autophagy, the Unc-51–like kinase and TANK-binding kinase (ULK) complex, which is composed of the ULK1/2 kinase, autophagy-related 13 (ATG13), ATG101, and 200-kDa focal adhesion kinase family kinase–interacting protein (FIP200)/RB1-inducible coiled-coil protein 1, plays a critical role in phagophore initiation by recruiting and phosphorylating multiple downstream factors (*4*, *5*, *7*, *8*). Then, the activated class III phosphatidylinositol 3-kinase complex I (PI3KC3-C1) generates phosphatidylinositol-3-phosphate (PI3P) to act in phagophore nucleation (*4*, *5*, *7*). Subsequently, the PI3P generated by PI3KC3-C1 can be specifically sensed by the downstream WD repeat domain phosphoinositide-interacting protein (WIPI) family proteins, which consist of four members in mammalian (WIPI1 to WIPI4) and can further recruit additional PI3KC3-C1 and other binding partners, such as ATG16L1 and ATG2A/2B, to promote phagophore elongation at the site of PI3P generation (*4*, *5*, *7*, *11*–*15*). Meanwhile, the two ubiquitin-like protein conjugation systems, the ATG5-ATG12 conjugation system and the ATG8 family proteins–phosphatidylethanolamine (PE) conjugation system, facilitate phagophore expansion and completion by catalyzing the PE lipidation of ATG8 family proteins (*4*, *5*, *7*, *16*). Specifically, in the ubiquitin-like protein conjugation systems, the ubiquitin-like ATG12 conjugates with ATG5 mediated by the E1-like ATG7 and E2-like ATG10, forming the ATG12~ATG5 conjugate, which can further associate with ATG16L1 to form the E3-like ATG12~ATG5-ATG16L1 complex for catalyzing the PE conjugation of ATG8 family proteins (*5*, *7*, *16*). Notably, the PE conjugation of ATG8 family proteins plays critical roles in autophagic vesicle trafficking and autophagosome-lysosome fusion except for autophagosome biogenesis (*16*–*19*). Although the core autophagic proteins are well demonstrated to be essential for canonical autophagy, many of the detailed molecular mechanisms underpinning the specific associations of these core autophagic proteins involved in the biogenesis of autophagosome are still largely unknown.

As a key autophagic protein, ATG16L1 contains an N-terminal ATG5-binding domain that is responsible for the interaction with ATG12~ATG5 conjugate to assemble the E3-like ATG12~ATG5-ATG16L1 complex (*20*) and a following membrane-binding motif (Fig. 1A), which is essential for the lipidation of ATG8 family proteins but not the targeting of the ATG12~ATG5-ATG16L1 complex to phagophore membrane (*21*). The middle region of ATG16L1 contains a coiled-coil domain (Fig. 1A), which can induce the self-dimerization of ATG16L1 and associate with Ras-related protein Rab-33 (RAB33) (*22*–*24*). In addition, the central region of ATG16L1 also harbors a WIPI2b-binding site and an FIP200-interacting region (FIR) motif (Fig. 1A), which can interact with FIP200 for the association with the ULK complex (*25*, *26*). Unlike its yeast homolog ATG16, the C-terminal region of ATG16L1 contains an additional WD40 repeat domain (Fig. 1A), which can specifically recognize invading pathogens or pathogen-containing vacuoles by binding to relevant proteins including ubiquitin (*27*), the complement protein C3 (*28*, *29*), and vacuolar-type adenosine triphosphatase (*30*), thereby endowing ATG16L1 with specific

[1]State Key Laboratory of Bio-Organic and Natural Products Chemistry, Center for Excellence in Molecular Synthesis, Shanghai Institute of Organic Chemistry, University of Chinese Academy of Sciences, Chinese Academy of Sciences, Shanghai 200032, China. [2]School of Chemistry and Materials Science, Hangzhou Institute for Advanced Study, University of Chinese Academy of Sciences, 1 Sub-lane Xiangshan, Hangzhou 310024, China.
*Corresponding author. Email: panlf@sioc.ac.cn

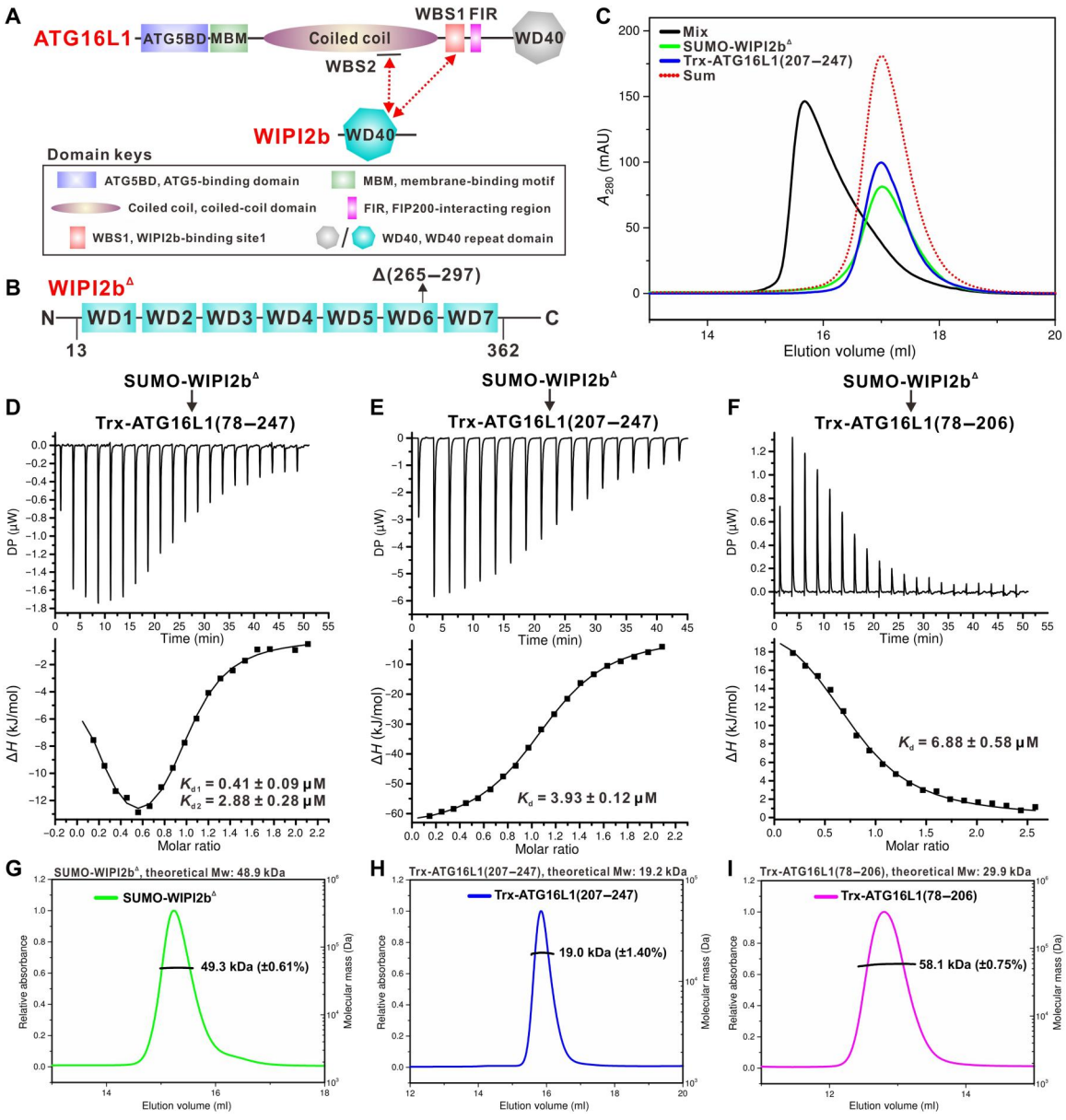

Fig. 1. Biochemical characterizations of the interaction between WIPI2b and ATG16L1ABCDFGI (**A**) The schematic diagram showing the domain organizations of ATG16L1 and WIPI2b. In this drawing, the interactions of ATG16L1 with WIPI2b are highlighted and indicated by two-way arrows. (**B**) The schematic diagram of WIPI2b$^{\Delta}$ (residues 13 to 362 without 265 to 297). (**C**) Analytic gel filtration chromatography–based analysis of the interaction of SUMO-tagged WIPI2b with Trx-tagged ATG16L1(207 to 247). In this panel, "Sum" stands for the theoretical sum of SUMO-WIPI2b and Trx-ATG16L1(207 to 247) profiles, while "Mixture" stands for the SUMO-WIPI2b and Trx-ATG16L1(207 to 247) mixture sample. (**D** to **F**) ITC-based measurement of the binding affinities of SUMO-tagged WIPI2b$^{\Delta}$ with Trx-tagged ATG16L1(78 to 247) (D), Trx-tagged ATG16L1(207 to 247) (E), and Trx-tagged ATG16L1(78 to 206) (F). The K_d values of SUMO-tagged WIPI2b$^{\Delta}$ with Trx-tagged ATG16L1(207 to 247) and ATG16L1(78 to 206) are the fitted dissociation constants with SEs when using one–binding site model to fit the ITC data. In particular, two K_d values of SUMO-tagged WIPI2b$^{\Delta}$ with Trx-tagged ATG16L1(78 to 247) are the fitted dissociation constants with SEs when using two–binding site model to fit the ITC data. "DP" is the differential power measured by the ITC machine. (**G** to **I**) Plots of the MALS data of the purified SUMO-WIPI2b$^{\Delta}$ (G), Trx-ATG16L1(207 to 247) (H), and Trx-ATG16L1(78 to 206) (I). The molecular mass errors are the fitted errors obtained from the data analysis software and are showed in the brackets. A_{280}, absorbance at 280 nm; mAU, milli–arbitrary units; Mw, molecular weight.

functions in antibacterial selective autophagy (also named xenophagy) (*31*). Notably, ATG16L1 is a well-proved phagophore marker (*32*), and its specific recruitment to phagophore membrane is mediated by relevant upstream autophagic proteins, such as WIPI2b and FIP200 (*11*, *25*, *26*). In particular, the direct interaction between PI3P-binding WIPI2b and ATG16L1 is considered to bridge PI3P production and the PE lipidation of ATG8 family proteins, two crucial steps in autophagosome formation. The interaction between ATG16L1 and WIPI2b is also required for xenophagy in addition to its essential role in canonical autophagy (*11*). However, the related molecular mechanism underlying the recognition of ATG16L1 by WIPI2b remains elusive. Previous studies well demonstrated that the removal of reported WIPI2b and FIP200 binding sites of ATG16L1 can largely reduce but not completely abolish the phagophore localization of ATG16L1 (*25*, *26*), suggesting the existence of additional uncharacterized mechanism for the recruitment of ATG16L1 to phagophore.

In this study, we systemically characterize the interaction between ATG16L1 and WIPI2b and find that the coiled-coil region of ATG16L1 also contains a WIPI2b-binding site, in addition to the previously reported WIPI2b-binding site. The determined high-resolution crystal structures of WIPI2b in complex with two different WIPI2b-binding sites of ATG16L1 not only uncover the detailed molecular mechanism governing the specific association of ATG16L1 with WIPI2b but also reveal that WIPI2b adopts the same pocket to recognize the two distinct WIPI2b-binding sites of ATG16L1. Furthermore, we elucidate that the previously unidentified WIPI2b-binding site of ATG16L1 and its binding mode with WIPI2b are highly conserved even in yeast. Last, using relevant cell-based assays, we functionally demonstrate that the integrity of two WIPI2b-binding sites of ATG16L1 is essential for the effective autophagic flux in starvation-induced autophagy.

RESULTS

The biochemical elucidation of the two different WIPI2b-binding sites of ATG16L1

To elucidate the molecular mechanism governing the interaction between WIPI2b and ATG16L1, we firstly sought to obtain relevant WIPI2b and ATG16L1 proteins for detailed biochemical and structural characterizations. However, after numerous trials, we failed to obtain soluble recombinant proteins of WIPI2b from *Escherichia coli* cells. A careful sequence alignment analysis of WIPI2b from different species together with relevant secondary structure predication and homology structure modeling by Protein Homology/analogy Recognition Engine 2 (Phyre2) server (*33*) revealed that there is a long loop insertion (residues 265 to 297) within the putative sixth blade of WIPI2b WD40 repeat domain (fig. S1). Notably, this insertion region contains a large portion of hydrophobic residues, and previous studies of SVP1-like protein 2 (Hsv2), a yeast homolog of WIPI protein, demonstrated that the corresponding region of Hsv2 can penetrate the membrane to promote the membrane binding of Hsv2 (*34*, *35*). Furthermore, loop truncation strategy was successfully used for crystallization of WIPI3 protein in a previous study (*36*). Therefore, we wondered whether we could delete this hydrophobic loop region of WIPI2b to facilitate its folding in *E. coli* cells. Thus, we designed a core WD40 construct of WIPI2b (hereafter referred to as WIPI2b$^{\Delta}$), in which the putative membrane-insertion region of WD40 repeat domain (residues 265 to 297) and the predicated unstructured N-terminal region (residues 1 to 12) and C-terminal region (residues 363 to 436) of WIPI2b were removed (Fig. 1B). Fortunately, using this WIPI2b$^{\Delta}$ construct, we could readily obtain soluble proteins of WIPI2b from *E. coli* cells despite a very lower expression level.

Then, using these soluble WIPI2b$^{\Delta}$ proteins, we sought to map out the precise WIPI2b-binding region of ATG16L1. On the basis of the sequence conservation and secondary structure predication of ATG16L1 together with the fact that residues 207 to 230 of ATG16L1 are required for the specific interaction between ATG16L1 and WIPI2b in cells (*11*), we chose three ATG16L1 fragments (residues 207 to 247, 78 to 247, and 78 to 206) and then purified these proteins. Using analytical gel filtration chromatography–based comigration assays, we revealed that the ATG16L1(207 to 247) and ATG16L1(78 to 247) fragments can readily interact with WIPI2b$^{\Delta}$ (Fig. 1C and fig. S3A), but unexpectedly, ATG16L1(78 to 206) that lacks the reported WIPI2b-binding region (residues 207 to 230) can also directly interact with WIPI2b$^{\Delta}$ (fig. S3B), suggesting that ATG16L1 might contain another site for interacting with WIPI2b. Further quantitative isothermal titration calorimetry (ITC)–based analyses revealed that the relatively long fragment ATG16L1(78 to 247) displays a two–binding site mode to interact with WIPI2b$^{\Delta}$ (Fig. 1D and table S1). In contrast, the short ATG16L1(207 to 247) and ATG16L1(78 to 206) fragments bind to WIPI2b$^{\Delta}$ by a one–binding site mode and with dissociation constant (K_d) values of ~3.9 and ~6.9 μM, respectively (Fig. 1, E and F, and table S1). Notably, the binding processes of ATG16L1(207 to 247) and ATG16L1(78 to 206) with WIPI2b$^{\Delta}$ showed opposite enthalpy changes (exothermic versus endothermic) in our ITC-based assays (Fig. 1, E and F), confirming that ATG16L1 has two distinct WIPI2-binding sites. Further multiangle light scattering (MALS) measurements showed that WIPI2b$^{\Delta}$ and ATG16L1(207 to 247) are monomers in solution (Fig. 1, G and H), while both ATG16L1(78 to 206) and ATG16L1(78 to 247) form dimers in solution (Fig. 1I and fig. S4). Therefore, in addition to the previously reported WIPI2b-binding site (hereafter referred to as WBS1), the dimeric coiled-coil region of ATG16L1 contains another WIPI2b-binding site (hereafter referred to as WBS2).

Biochemical mapping of the WBS1 boundary within ATG16L1

Next, we intended to determine the crystal structure of WIPI2b$^{\Delta}$ in complex with ATG16L1 fragment containing both WIPI2b-binding sites. However, we failed to crystallize this complex, likely because of its dynamic nature. As an alternative, we sought to determine the complex structure of WIPI2b$^{\Delta}$ with separated WBS1 or WBS2 of ATG16L1. We firstly focused on the interaction between WIPI2b and the WBS1 of ATG16L1. To precisely map out the minimal boundary of ATG16L1 WBS1 for further structural study, we constructed another four ATG16L1 fragments (residues 186 to 236, 207 to 236, 213 to 236, and 221 to 236), then purified these proteins, and performed ITC assays to quantitatively compare their interactions with WIPI2b$^{\Delta}$. Our ITC results revealed that ATG16L1(207 to 236), ATG16L1(186 to 236), and ATG16L1(207 to 247) fragments bind to WIPI2b$^{\Delta}$ with similar K_d values (Figs. 1E and 2F; fig. S5, A and B; and table S1), while ATG16L1(213 to 236) (Fig. 2F, fig. S5C, and table S1) has a much reduced binding affinity toward WIPI2b$^{\Delta}$, and ATG16L1(221 to 236) even cannot interact with WIPI2b$^{\Delta}$

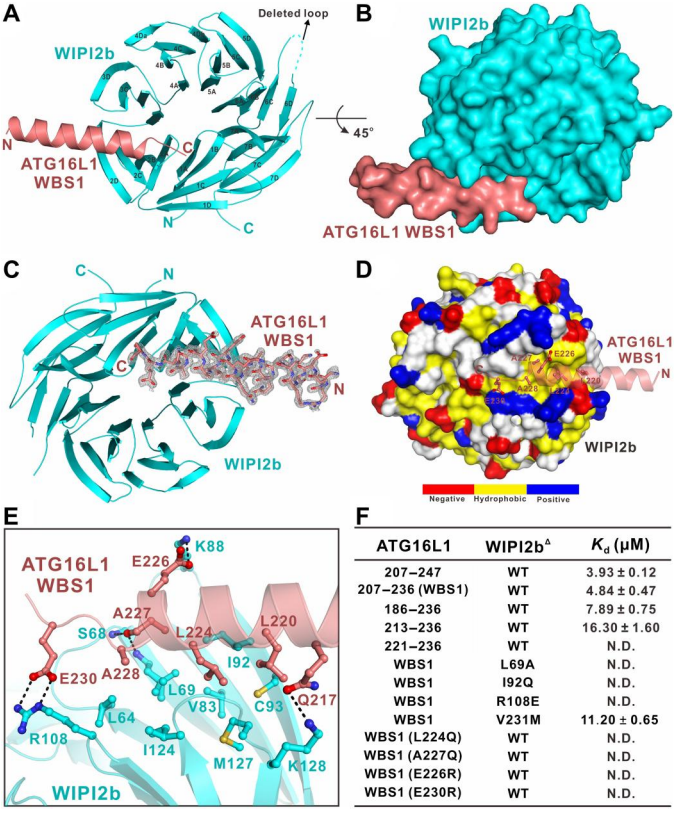

F

ATG16L1	WIPI2b$^{\Delta}$	K_d (μM)
207–247	WT	3.93 ± 0.12
207–236 (WBS1)	WT	4.84 ± 0.47
186–236	WT	7.89 ± 0.75
213–236	WT	16.30 ± 1.60
221–236	WT	N.D.
WBS1	L69A	N.D.
WBS1	I92Q	N.D.
WBS1	R108E	N.D.
WBS1	V231M	11.20 ± 0.65
WBS1 (L224Q)	WT	N.D.
WBS1 (A227Q)	WT	N.D.
WBS1 (E226R)	WT	N.D.
WBS1 (E230R)	WT	N.D.

Fig. 2. The molecular mechanism of WIPI2b and ATG16L1 WBS1 interaction. (**A**) The ribbon diagram showing the overall structure of the WIPI2b$^{\Delta}$/ATG16L1 WBS1 complex. In this drawing, WIPI2b$^{\Delta}$ and ATG16L1 WBS1 are shown in cyan and deep salmon, respectively. (**B**) The surface representation showing the overall architecture of WIPI2b$^{\Delta}$/ATG16L1 WBS1 complex with the same color scheme as that in (A). (**C**) The 2mFo-DFc map of ATG16L1 WBS1 in the structure of the WIPI2b$^{\Delta}$/ATG16L1 WBS1 complex showing that the electron densities of ATG16L1 WBS1 can be clearly assigned. The electron density map is calculated by omitting the ATG16L1 WBS1 peptide from the final PDB file and contoured at 1.6σ. (**D**) The combined surface representation and the ribbon-stick model showing the hydrophobic binding surface between WIPI2b$^{\Delta}$ and ATG16L1 WBS1. In this drawing, ATG16L1 WBS1 is displayed as a ribbon-stick model and WIPI2b$^{\Delta}$ is showed in the surface representation colored by different amino acid types. Specifically, the hydrophobic amino acid residues in the surface model of WIPI2b$^{\Delta}$ are drawn in yellow. The positively charged residues are drawn in blue. The negatively charged residues in are drawn red, and the uncharged polar residues are drawn in gray. (**E**) The ribbon-stick model showing the detailed interactions between WIPI2b$^{\Delta}$ and ATG16L1 WBS1. The hydrogen bonds and salt bridges involved in the binding are shown as dotted lines. (**F**) The measured binding affinities between different WIPI2b$^{\Delta}$ and ATG16L1 variants by ITC-based binding assays. "N.D." stands for when the K_d value is not detectable. WT, wild type.

(Fig. 2F and fig. S5D). Collectively, we concluded that the WBS1 of ATG16L1 is located within the ATG16L1(207 to 236) region.

The structure of WIPI2b$^{\Delta}$ in complex with ATG16L1 WBS1

Using the purified WIPI2b$^{\Delta}$ and ATG16L1 WBS1 complex, we successfully obtained good crystals that diffracted to 1.50 Å. Using the molecular replacement method with the modified WD40 structure of yeast ATG18 [Protein Data Bank (PDB) ID: 5LTG], we determined the crystal structure of the WIPI2b$^{\Delta}$/ATG16L1 WBS1 complex (table S2). In the final complex structural model, an asymmetric unit contains one WIPI2b$^{\Delta}$/ATG16L1 WBS1 complex, which forms a 1:1 stoichiometric binary complex (Fig. 2, A and B). As expected, WIPI2b$^{\Delta}$ in the complex structure adopts a typical WD40 repeat folding, featuring a seven-bladed β-propeller architecture (Fig. 2A), and the overall structure of WIPI2b in the WIPI2b$^{\Delta}$/ATG16L1 complex is similar to that of the *apo*-form structures of Hsv2 and WIPI3 (fig. S6, A and B). Notably, the clearly defined WBS1 of ATG16L1 in the complex structure contains 23 highly conserved residues (residues 209 to 231) and mainly forms a continuous α helix (Fig. 2, A and C, and fig. S2), which packs extensively with a solvent-exposed groove between the blades 2 and 3 of WIPI2b, burying a total of ~550-Å^2 surface area (Fig. 2B). Note that a similar overall architecture was also observed in a recently reported structure of the WIPI2d/ATG16L1(207 to 230) complex (*37*). Further structural analysis showed that WIPI2b contains the signature "FRRG" motif and forms two phosphoinositide-binding sites in the blade 5 and blade 6 regions (fig. S6, C and D), similar to other PROPPIN (β-propellers that bind polyphosphoinositides) family proteins (*34*–*36*). The phosphoinositide-binding sites and the ATG16L1-binding site are located in the opposite sides of the WD40 repeat domain of WIPI2b (fig. S6, C and D), in accord with the fact that WIPI2b can simultaneously associate with membrane and recruit the ATG12~ATG5-ATG16L1 complex (*11*). Notably, the deleted hydrophobic loop region of WIPI2b is far away from the ATG16L1-binding site (Fig. 2A). Therefore, it is unlikely to affect the interaction between WIPI2b and ATG16L1. Further structural comparison analyses revealed that although both WIPI2b and WIPI3 rely on a similar groove between the blades 2 and 3 of WD40 repeats to recognize their binding partners, the overall binding mode of WIPI2b with ATG16L1 is completely different from that of WIPI3 and ATG2A interaction (Fig. 2A and fig. S6, E and F).

Further detailed structural analyses of the molecular interface of WIPI2b$^{\Delta}$/ATG16L1 WBS1 complex revealed that the ATG16L1 helix binds to a highly electropositive and hydrophobic groove between blades 2 and 3 of WIPI2b (Fig. 2D and fig. S7A), and the specific interaction between WIPI2b and ATG16L1 is mainly mediated by extensive hydrophobic contacts and polar interactions (Fig. 2, D and E, and fig. S7A). Specifically, the hydrophobic side chains of L220, L224, A227, and A228 of ATG16L1 occupy a hydrophobic groove formed by the side chains of L64, L69, V83, I92, C93, I124, and M127 from WIPI2b (Fig. 2E). Concurrently, the polar side-chain group of Q217 and the backbone carboxyl group of A227 from ATG16L1 respectively interact with the K128, S68, and L69 residues of WIPI2b, forming three specific hydrogen bonds (Fig. 2E). In addition, the WIPI2b$^{\Delta}$/ATG16L1 complex is further stabilized by a E-K pair (E226$_{ATG16L1}$-K88$_{WIPI2b}$) and a E-R pair (E230$_{ATG16L1}$-R108$_{WIPI2b}$) of salt bridges (Fig. 2E and fig. S7A). In line with their important structural roles, all of these key residues of ATG16L1 and WIPI2b involved in the binding interface are strictly conserved across different eukaryotic species (figs. S1 and S2). Using ITC method, we further validated the specific interactions between ATG16L1 and WIPI2b observed in the complex structure. Consistent with our structural data, point mutations of key interface residues either from WIPI2b or ATG16L1, such as the L69A, I92Q, and R108E mutations of WIPI2b or the L224Q, E226R, A227Q, and E230R mutations of ATG16L1, all disrupted the interaction between ATG16L1(207 to 236) and WIPI2b$^{\Delta}$ in our ITC-based assays (Fig. 2F and figs. S8 and S9). In contrast,

the disease-associated WIPI2b V231M missense mutation (*38*), which is located in the phosphoinositide-binding region of WIPI2b (fig. S7B), had a mild effect on the interaction of WIPI2b$^{\Delta}$ and ATG16L1 WBS1 (Fig. 2F, fig. S8E, and table S1).

The overall structure of the WIPI2b$^{\Delta}$/ATG16L1 WBS2 complex

Then, we also decided to structurally characterize the interaction between WIPI2b$^{\Delta}$ and the previously unidentified WBS2 of ATG16L1. Unfortunately, initial crystallization attempts using the ATG16L1(78 to 206)/WIPI2b$^{\Delta}$ complex failed. Therefore, we further truncated the C-terminal part of ATG16L1(78 to 206) and constructed an ATG16L1(78 to 197) fragment. Our MALS and ITC analyses revealed that ATG16L1(78 to 197) can still form a stable dimer in solution (fig. S10A) and binds to WIPI2b$^{\Delta}$ with a similar affinity in comparison with ATG16L1(78 to 206) (Figs. 1F and 3F, fig. S10B, and table S1). Using the purified WIPI2b$^{\Delta}$/ATG16L1(78 to 197) complex, we successfully obtained crystals that diffracted to ~4-Å resolution. We managed to solve this low-resolution complex structure and found that the extreme N-terminal 45 residues (residues 78 to 123) of ATG16L1(78 to 197) does not show any defined electron density in the crystal structure, suggesting the flexible property of this N-terminal region. Consistent with this observation, further MALS analysis revealed that ATG16L1(78 to 125) adopts a monomeric rather than dimeric state (fig. S10C). To improve the quality of this complex structure, we further narrowed down the N-terminal boundary of ATG16L1(78 to 197) and crystallized the WIPI2b$^{\Delta}$/ATG16L1(124 to 197) complex. Unexpectedly, this N-terminal truncation of ATG16L1 resulted under much more crystal-growing conditions but no improvement of the crystal structure resolution. Notably, most crystals of the WIPI2b$^{\Delta}$/ATG16L1(78 to 197) and WIPI2b$^{\Delta}$/ATG16L1(124 to 197) complexes from different crystallization conditions shared the same space group $P6_122$, and the extreme C-terminal part (residues 189 to 195) of ATG16L1(78 to 197) in the WIPI2b$^{\Delta}$/ATG16L1(124 to 197) complex structure is directly involved in the crystal packing but does not participate in the interaction with WIPI2b$^{\Delta}$ (fig. S10, D and E). Therefore, we wondered whether we could remove this C-terminal part of ATG16L1(124 to 197) to change the crystal packing for improving the crystal quality. Fortunately, using the WIPI2b$^{\Delta}$/ATG16L1(124 to 188) complex, we eventually harvested good crystals, which grew in the $P12_11$ space group and were diffracted to 1.76-Å resolution (table S2).

Using the molecular replacement method, we determined the WIPI2b$^{\Delta}$/ATG16L1(124 to 188) complex structure (table S2), which consists of two WIPI2b$^{\Delta}$ molecules and one ATG16L1(124 to 188) dimer, forming a unique 2:2 stoichiometric heterotetramer (Fig. 3, A and B). In the complex structure, two ATG16L1(124 to 188) molecules mainly adopt two continuous α helices and pack with each other in a head-to-head manner to form a parallel coiled-coil dimer (Fig. 3, A and B). As expected, two WIPI2b$^{\Delta}$ molecules fold as canonical WD40 repeats and symmetrically bind to the middle region of the dimeric ATG16L1(124 to 188) coiled coil (Fig. 3, A and B). Notably, there is no direct contact between two WIPI2b$^{\Delta}$ molecules in the complex structure (Fig. 3, A and B). Apparently, the overall binding mode of WIPI2b$^{\Delta}$ with ATG16L1(124 to 188) is quite different from that of WIPI2b$^{\Delta}$ with WBS1 (Figs. 3A and 2A).

The molecular interfaces in the WIPI2b$^{\Delta}$/ATG16L1 WBS2 complex structure

In the determined WIPI2b$^{\Delta}$/ATG16L1(124 to 188) complex structure, there are two distinct types of binding interfaces, the dimerization interface of ATG16L1 coiled coil and the WIPI2b$^{\Delta}$/ATG16L1(124 to 188) binding interface (Fig. 3, C and E). In particular, the dimerization of ATG16L1 coiled coil is mediated by extensive hydrophobic contacts and sporadic polar interactions between residues located at the a, b, d, and e positions of the two ATG16L1 helices (residues 127 to 187), each of which is composed of eight regular heptad repeats (Fig. 3C and fig. S11, A and B). Specifically, an N-terminal hydrophobic patch assembled by the K130, I131, C134, T137, I138, L141, C145, L148, K151, L152, and L155 residues, together with a C-terminal hydrophobic patch formed by the L162, K163, Y166, L169, F173, L176, L180, and T183 residues from one helical ATG16L1 chain, has hydrophobic contacts with the corresponding counterpart in another chain of the dimeric ATG16L1 (Fig. 3C and fig. S11, A and B). In addition, two highly specific hydrogen bonds are found between the side chains of two N159 residues and two N187 residues located in the middle region and the C-terminal region of the paired ATG16L1 helices, respectively (Fig. 3C and fig. S11B). Furthermore, two symmetrical salt bridges formed between the negatively charged E144 of one ATG16L1 helix and the positively charged R149 of another ATG16L1 helix further stabilize the dimeric ATG16L1 coiled coil (Fig. 3C and fig. S11B).

Further structural analysis revealed that in the complex structure, two WIPI2b$^{\Delta}$ symmetrically bind to two opposite homodimeric interfaces located at the middle region of the ATG16L1 WBS2 helices, each burying a total of ~554-Å^2 surface area (Fig. 3, A and B). Detailed structural analysis uncovered that the binding interface between WIPI2b$^{\Delta}$ and the dimeric ATG16L1 is mainly formed by residues from the blades 2 and 3 of WIPI2b, which accommodates ATG16L1 residues located in the middle region of the dimeric ATG16L1 helices through both polar and hydrophobic interactions (Fig. 3, D and E, and fig. S11C). In particular, the side chains of Q160 and E165 residues from one helical ATG16L1 chain and the side chain of Q170 from another chain of the ATG16L1 dimer couple with the R108, S68, and K88 residues of WIPI2b to form four specific hydrogen bonds (Fig. 3E). In addition, the negatively charged D164 and D167 residues of ATG16L1 form charge-charge interactions and hydrogen bonds with the positively charged R108 and R125 residues of WIPI2b (Fig. 3, D and E). Concurrently, the hydrophobic side chains of A168, I171, and A175 of ATG16L1 occupy the hydrophobic groove formed by the side chains of L64, L69, I92, and I124 from WIPI2b (Fig. 3E and fig. S11C). Moreover, the side chain of T172 from one chain of the ATG16L1 dimer, together with the hydrophobic side chain of F173 from another chain, forms hydrophobic contacts with the methyl group of T90 and the aliphatic side chain of K88 from WIPI2b (Fig. 3E and fig. S11C). In accordance with their crucial structural roles, all these key interface residues of WIPI2b and ATG16L1 WBS2 are highly conserved during evolution (figs. S1 and S2). Using ITC-based assays, we further validated the specific interactions between WIPI2b and ATG16L1 WBS2 observed in the complex structure (figs. S12 and S13 and table S1). In agreement with the aforementioned structural data, individual point mutations of key residues involved in the binding interface of the WIPI2b$^{\Delta}$/ATG16L1 WBS2 complex either from WIPI2b$^{\Delta}$ or ATG16L1, such as the L69A, K88A, I92Q, R108E, and I124Q mutations of

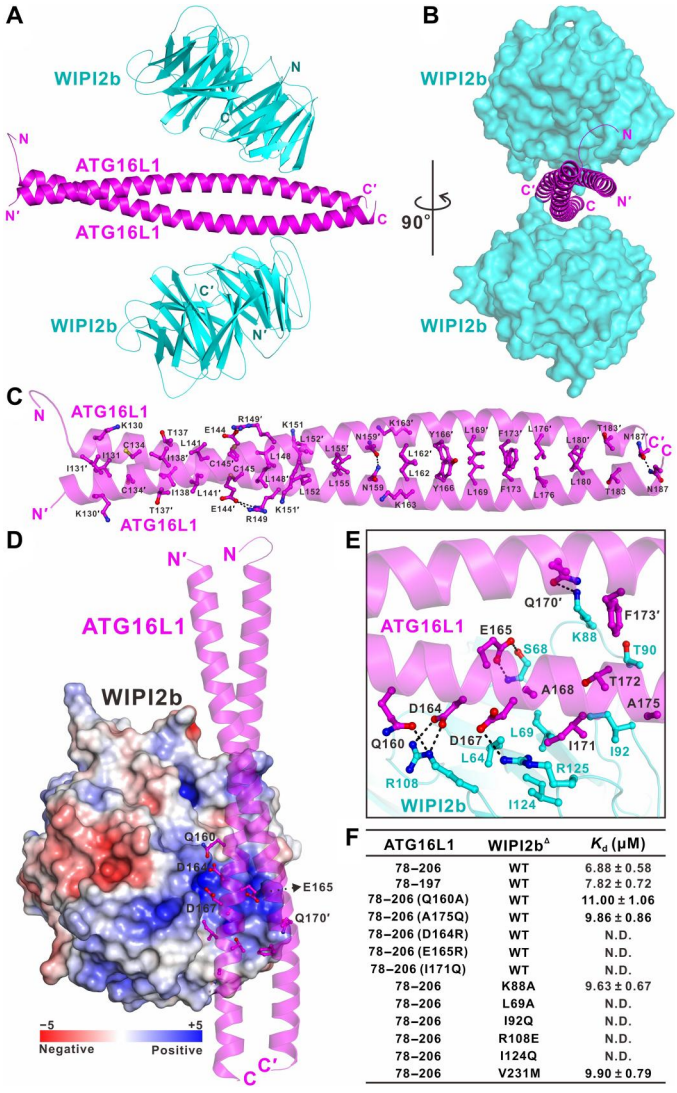

F

ATG16L1	WIPI2b$^{\Delta}$	K_d (μM)
78–206	WT	6.88 ± 0.58
78–197	WT	7.82 ± 0.72
78–206 (Q160A)	WT	11.00 ± 1.06
78–206 (A175Q)	WT	9.86 ± 0.86
78–206 (D164R)	WT	N.D.
78–206 (E165R)	WT	N.D.
78–206 (I171Q)	WT	N.D.
78–206	K88A	9.63 ± 0.67
78–206	L69A	N.D.
78–206	I92Q	N.D.
78–206	R108E	N.D.
78–206	I124Q	N.D.
78–206	V231M	9.90 ± 0.79

Fig. 3. The molecular mechanism of WIPI2b and ATG16L1 WBS2 interaction. (**A**) The ribbon diagram showing the overall structure of the WIPI2b$^{\Delta}$/ATG16L1 WBS2 complex. In this drawing, WIPI2b$^{\Delta}$ and ATG16L1 WBS2 are shown in cyan and magenta, respectively. (**B**) The combined surface representation and the ribbon-stick model showing the overall architecture of WIPI2b$^{\Delta}$/ATG16L1 WBS2 complex. In this drawing, ATG16L1 is displayed in the ribbon-stick model and WIPI2b$^{\Delta}$ is showed in the surface representation colored as that in (A). (**C**) The ribbon-stick model showing the detailed dimerization interface of the ATG16L1 coiled coil in the WIPI2b$^{\Delta}$/ATG16L1 WBS2 complex structure. In this drawing, the hydrogen bonds and salt bridges involved in the binding are shown as dotted lines. (**D**) The combined surface charge representation and the ribbon-stick model showing the charge-charge interactions between WIPI2b$^{\Delta}$ and ATG16L1 WBS2. (**E**) The ribbon-stick model showing the detailed interactions between WIPI2b$^{\Delta}$ and ATG16L1 WBS2. The hydrogen bonds and salt bridges involved in the binding are shown as dotted lines. (**F**) The measured binding affinities between WIPI2b$^{\Delta}$ and different ATG16L1 fragments or their mutants by ITC-based binding assays. "N.D." stands for when the K_d value is not detectable.

WIPI2b or the Q160A, D164R, E165R, I171Q, and A175Q mutations of ATG16L1(78 to 206), all decreased or essentially abolished the specific interaction between WIPI2b$^{\Delta}$ and ATG16L1(78 to 206) (Fig. 3F and figs. S12 and S13). As expected, the disease-associated WIPI2b V231M missense mutation had a subtle effect on the interaction of WIPI2b$^{\Delta}$ and ATG16L1(78 to 206) (Fig. 3F and fig. S13G).

The relationship of ATG16L1 WBS1 and WBS2 in binding to WIPI2b

Further structural comparison analysis showed that although both WBS1 and WBS2 of ATG16L1 use helical structures to associate with WIPI2b$^{\Delta}$, the orientations of these helices are running in the opposite direction (Fig. 4A). Despite the fact that ATG16L1 WBS1 and WBS2 adopt different binding modes to interact with WIPI2b, they actually occupy the same pocket of WIPI2b (Fig. 4A). Notably, WIPI2b uses many identical interface residues to interact with both WBS1 and WBS2 of ATG16L1, such as L64, L69, K88, I92, and R108 (Figs. 2E and 3E and fig. S1). Therefore, ATG16L1 WBS1 and WBS2 should be unable to simultaneously interact with the same WIPI2b because of potential steric exclusion. Our analytical gel filtration chromatography coupled with SDS–polyacrylamide gel electrophoresis (PAGE) analyses revealed that the isolated ATG16L1(207 to 236) and ATG16L1(78 to 206) are competitive in binding to WIPI2b$^{\Delta}$ (fig. S14). Recently, the crystal structure of RAB33B in complex with ATG16L1(141 to 225) that contains portions of WBS1 and WBS2 of ATG16L1 was reported (*23*). Further structural modeling analysis using our determined structures of ATG16L1(207 to 236)/WIPI2b$^{\Delta}$ and ATG16L1(124 to 188)/WIPI2b$^{\Delta}$ complexes, together with the ATG16L1(141 to 225)/RAB33B complex structure (PDB ID: 6Y09), showed that ATG16L1 WBS1 and WBS2 are spatially far away from each other and should be able to simultaneously interact with different WIPI2b molecules (Fig. 4B), in accordance with our aforementioned ITC result that WBS1 and WBS2 within the ATG16L1(78 to 247) fragment can fully participate in the association with WIPI2b$^{\Delta}$ to present a two–binding site mode (Fig. 1D). To further elucidate the relationship of WBS1 and WBS2 in the context of the same ATG16L1 fragment when engaging with WIPI2b, we conducted relevant MALS-based assays using the ATG16L1(124 to 247) fragment that contains intact WBS1 and WBS2 of ATG16L1. The MALS results showed that ATG16L1(124 to 247) forms a stable dimer and can specifically interact with the monomeric WIPI2b$^{\Delta}$ to form binary complexes with inhomogeneous molecular weight distributions but likely having a major species with a 2:2 rather than anticipated 2:4 stoichiometry in solution (fig. S15). Nevertheless, it is convincing that WBS1 and WBS2 of ATG16L1 can simultaneously interact with different WIPI2b molecules in vitro.

The validation of ATG16L1 WBS1 and WBS2 for binding to WIPI2b in vitro and in cells

To further validate the specific interactions of WIPI2b with ATG16L1 WBS1 and WBS2 observed in our structural characterizations, we conducted relevant mutagenesis-based assays. Using ITC-based analyses, we demonstrated that point mutations of key interface residues within the WBS2 of ATG16L1(78 to 247), such as the D164R and I171Q mutations, completely disrupted the interaction of WIPI2b$^{\Delta}$ with the WBS2 of ATG16L1(78 to 247) but had no obvious effects on the interaction between WIPI2b$^{\Delta}$ and the WBS1 of ATG16L1(78 to 247) (Fig. 4C; fig. S16, A and B; and

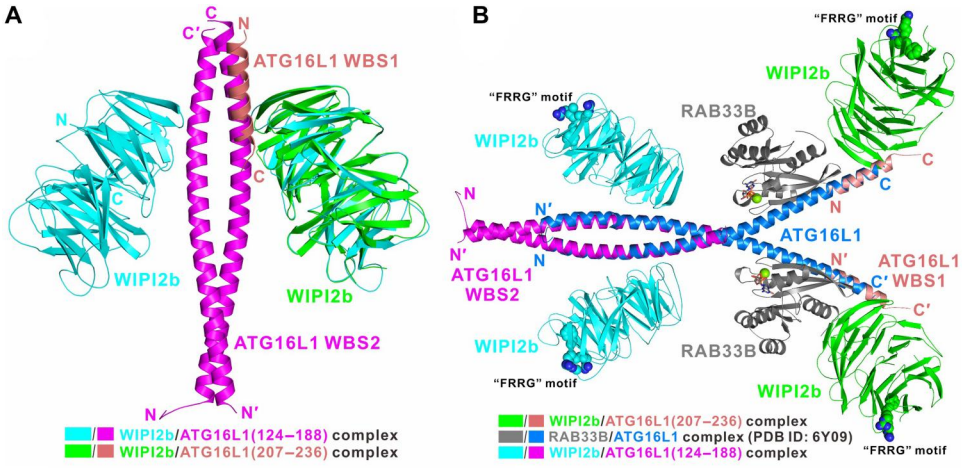

C

ATG16L1 proteins	WIPI2b$^{\Delta}$	K_d (μM)
WBS1	WT	4.84 ± 0.47
78–206	WT	6.88 ± 0.58
78–247	WT	0.41 ± 0.09/2.88 ± 0.28
78–247 (D164R)	WT	4.30 ± 0.41
78–247 (I171Q)	WT	4.00 ± 0.25
78–247 (L224Q)	WT	9.36 ± 1.31
78–247 (A227Q)	WT	9.26 ± 1.01
78–247 (D164R/L224Q)	WT	N.D.
78–247 (D164R/A227Q)	WT	N.D.
78–247 (D164R)/RAB33B complex	WT	5.46 ± 0.37
78–247 (L224Q)/RAB33B complex	WT	5.64 ± 0.45

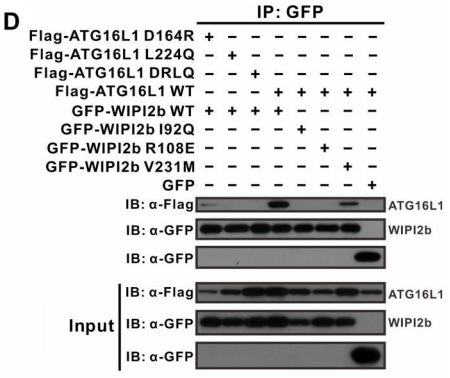

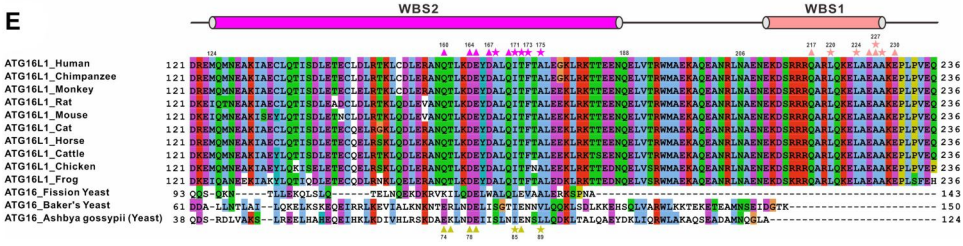

Fig. 4. The comparison between ATG16L1 WBS1 and WBS2 on the association with WIPI2b. (**A**) The structural comparison of the WIPI2b$^{\Delta}$/ATG16L1 WBS1 and WIPI2b$^{\Delta}$/ATG16L1 WBS2 complexes. In this drawing, the WIPI2b$^{\Delta}$ molecules in the WIPI2b$^{\Delta}$/ATG16L1 WBS1 complex and the WIPI2b$^{\Delta}$/ATG16L1 WBS2 complex are shown in green and cyan, respectively. (**B**) A structural modeling of ATG16L1 WBS1 and WBS2 within the same ATG16L1 coiled coil in binding to WIPI2b based on the structures of the WIPI2b$^{\Delta}$/ATG16L1 WBS1 complex, the WIPI2b$^{\Delta}$/ATG16L1 WBS2 complex, and the previously reported RAB33B/ATG16L1(141 to 225) complex (PDB ID: 6Y09). In this modeling, the two WIPI2b$^{\Delta}$/ATG16L1 WBS1 and WIPI2b$^{\Delta}$/ATG16L1 WBS2 complex structures are aligned to the RAB33B/ATG16L1(141 to 225) complex structure on the basis of the overlapped ATG16L1 helical regions. Meanwhile, the four residues comprising the WIPI2b FRRG motif for binding to PI3P are all highlighted in the sphere mode. (**C**) The measured binding affinities between WIPI2b$^{\Delta}$ and different ATG16L1 fragments or ATG16L1 variants by ITC-based assays. "N.D." stands for when the K_d value is not detectable. (**D**) Coimmunoprecipitation assays showing that point mutations of key interface residues of WIPI2b or ATG16L1 observed in the WIPI2b$^{\Delta}$/ATG16L1 WBS1 and WIPI2b$^{\Delta}$/ATG16L1 WBS2 complex structures decrease or essentially disrupt their specific interaction in cells, while the disease-associated V231M mutation of WIPI2b slightly impairs the association of WIPI2b with ATG16L1. "IB" means immunoblotting. (**E**) Structure-based sequence alignment of ATG16 and ATG16L1 from different species. The conserved residues are highlighted by colors using software Jalview 2.10.5 (www.jalview.org/). In this alignment, the conserved interface residues of ATG16L1 WBS1 and WBS2 involved in the interactions with WIPI2b and the conserved interface residues of *A. gossypii* ATG16 involved in the interaction with *K. lactis* ATG21 in the ATG21/ATG16 complex structure (PDB ID: 6RGO) are respectively highlighted with deep salmon, magenta, and yellow stars (hydrophobic interactions) or triangles (polar interactions). IP, immunoprecipitation.

table S1). Conversely, mutations of key interface residues within the WBS1 of ATG16L1(78 to 247), such as the L224Q and A227Q mutations, essentially eliminated the interaction of WIPI2b$^{\Delta}$ with the WBS1 of ATG16L1(78 to 247) but had little effect on the WIPI2b$^{\Delta}$/ATG16L1(78 to 247) WBS2 interaction (Fig. 4C; fig. S16, C and D; and table S1). Simultaneous mutations of key interface residues within the WBS1 and WBS2 of ATG16L1(78 to 247), such as the D164R/L224Q and D164R/A227Q double mutations, completely abolished the binding of ATG16L1(78 to 247) with WIPI2b$^{\Delta}$ (Fig. 4C and fig. S16, E and F).

To further validate the relationship of ATG16L1 WBS1 and WBS2 in binding to WIPI2b, we also generated four heterodimers of ATG16L1(124 to 247) with relevant D164R and L224Q mutations including the ATG16L1(124 to 247) wild-type (WT)/

ATG16L1(124 to 247) D164R/L224Q heterodimer, the ATG16L1(124 to 247) L224Q/ATG16L1(124 to 247) D164R heterodimer, the ATG16L1(124 to 247) D164R/ATG16L1(124 to 247) D164R/L224Q heterodimer, and the ATG16L1(124 to 247) L224Q/ATG16L1(124 to 247) D164R/L224Q heterodimer (fig. S17, A, D, G, and J). Further MALS-based assays using these heterodimers of ATG16L1(124 to 247) with two different molar ratios of WIPI2b$^{\Delta}$ showed that the ATG16L1(124 to 247) D164R/ATG16L1(124 to 247) D164R/L224Q and ATG16L1(124 to 247) L224Q/ATG16L1(124 to 247) D164R/L224Q heterodimers, which contain only one functional WBS1 or WBS2 site, can very weakly bind to WIPI2b (fig. S17, H, I, K, and L), while the ATG16L1(124 to 247)/ATG16L1(124 to 247) D164R/L224Q and ATG16L1(124 to 247) L224Q/ATG16L1(124 to 247) D164R heterodimers, which contain two functional WBS1 and WBS2 sites either on a single WT ATG16L1 chain or two mutated ATG16L1 chains, can more effectively interact with WIPI2b to form complexes with inhomogeneous molecular weight distributions but likely having a major species with a 1:1 stoichiometry in solution (fig. S17, B, C, E, and F). On the basis of these MALS results, we concluded that different WIPI2b proteins can simultaneously bind to the same ATG16L1 chain or two different ATG16L1 chains within the ATG16L1 dimer despite the fact that the interaction between WIPI2b and ATG16L1 WBS2 is much more dynamic than that of the WIPI2b/ATG16L1 WBS1 interaction in solution.

In agreement with the aforementioned biochemical and structural data (Figs. 2 and 3), further coimmunoprecipitation assays showed that point mutations of key binding interface residues of WIPI2b, such as the I92Q and R108E mutations, completely disrupted the binding of the full-length WIPI2b and ATG16L1 in cells (Fig. 4D). Meanwhile, the disease-associated V231M mutation of WIPI2b slightly decreased the specific interaction between WIPI2b and ATG16L1 (Fig. 4D). The ATG16L1 D164R mutation that can specifically disrupt the ATG16L1 WBS2/WIPI2b interaction in vitro, largely reduced the association of ATG16L1 with WIPI2b in cells, while the L224Q mutation that can specifically eliminate the ATG16L1 WBS1/WIPI2b interaction essentially abrogated the specific association of WIPI2b and ATG16L1 in cells (Fig. 4D). Concomitantly, the ATG16L1 D164R/L224Q double mutation that can eliminate both ATG16L1 WBS1/WIPI2b and ATG16L1 WBS2/WIPI2b interactions in vitro, also completely abolished the specific interaction between the full-length ATG16L1 and WIPI2b in cells (Fig. 4D).

The different conservation properties of ATG16L1 WBS1 and WBS2 from yeast to mammals

Budding yeast has three WIPI-related proteins—ATG18, ATG21, and Hsv2—of which ATG21 is known to interact with the yeast ATG16 for recruiting the E3-like ATG12~ATG5-ATG16 complex to the phagophore, similar to the WIPI2b/ATG16L1 pair in mammals (*10*). Previously, a 3.7-Å resolution crystal structure of *Kluyveromyces lactis* ATG21 in complex with the dimeric coiled coil of *Ashbya gossypii* ATG16 (PDB ID: 6RGO) was reported (*39*). Structural comparison analyses uncovered that the binding mode of the ATG16L1 WBS2/WIPI2b interaction but not the ATG16L1 WBS1/WIPI2b interaction resembles that of the yeast ATG16/ATG21 interaction (fig. S18, A and B). Further detailed structure and sequence alignment analyses showed that the ATG16L1 WBS2 site is evolutionarily conserved from yeast to mammals, while the ATG16L1 WBS1 site is totally absent in yeast ATG16 (Fig. 4E and fig. S18C). Notably, some key interface residues of ATG16L1 WBS2 for binding to WIPI2b, such as D164, E165, and I171, are strictly conserved during evolution (Fig. 4E and fig. S18C), implying a potentially pivotal role of ATG16L1 WBS2 in mammalian autophagy.

The essential roles of ATG16L1 WBS1 and WBS2 for the effective autophagic flux in canonical autophagy

To investigate the functional roles of ATG16L1 WBS1 and WBS2 in autophagy, we firstly generated an *ATG16L1*-knockout HeLa cell line using CRISPR-Cas9 technology (Fig. 5A and fig. S19). Then, *ATG16L1*-knockout HeLa cells were transfected with different lentiviruses to generate specific cell lines with stable expression of *Aequorea coerulescens* green fluorescent protein 1 (AcGFP1)–tagged WT ATG16L1, ATG16L1 D164R mutant (D164R) that loses the functional WBS2, ATG16L1 L224Q mutant (L224Q) that loses the functional WBS1, or ATG16L1 D164R/L224Q mutant (DRLQ) that loses both WBS1 and WBS2 for binding to WIPI2b. Subsequently, autophagic fluxes of these cell lines were assessed by measuring the Sequestosome-1 (SQSTM1)/p62 degradation and Microtubule-associated proteins 1A/1B light chain 3B (LC3B) lipidation levels under different conditions. As expected, the knockout of *ATG16L1* essentially blocked the autophagic flux either under a nutrient-rich or starvation condition, which can be well rescued by ATG16L1 WT (Fig. 5, A to D). Concurrently, both ATG16L1 D164R and ATG16L1 L224Q can partially restore starvation-induced LC3B lipidation and p62 degradation in *ATG16L1*-knockout cells (Fig. 5, C and D). Notably, ATG16L1 L224Q rather than ATG16L1 D164R is more effective to rescue the autophagic flux in *ATG16L1*-knockout cells (Fig. 5, C and D), underscoring an indispensable role of ATG16L1 WBS2 in starvation-induced autophagy. ATG16L1 D164R/L224Q is completely unable to rescue the autophagic flux in *ATG16L1*-knockout cells (Fig. 5, C and D). Consistently, further immunofluorescence microscopy–based assays showed that the *ATG16L1*-knockout cells rescued with ATG16L1 WT have normal autophagic fluxes with reasonable LC3B and ATG16L1 puncta formations under a starved but not a fed condition, while the ATG16L1 D164R/L224Q mutant is completely unable to restore starvation-induced puncta formation of LC3B and ATG16L1 (fig. S20, A to D). Meanwhile, ATG16L1 D164R and ATG16L1 L224Q mutants can only weakly and partially restore starvation-induced autophagic fluxes in ATG16L1-knockout cells, as only a few LC3B puncta can be observed in ATG16L1-knockout cells rescued with ATG16L1 D164R or L224Q mutant (fig. S20, A to C). Together, all these functional data indicated that the integrity of WBS1 and WBS2 of ATG16L1 is essential for the effective autophagic flux in starvation-induced autophagy.

DISCUSSION

Previous functional studies have well demonstrated that the four mammalian WIPI proteins can be classified into two subgroups: the WIPI1/2 group and the WIPI3/4 group, which can specifically recognize ATG16L1 and ATG2A/B, respectively (*11*–*13*, *15*). The molecular mechanism governing the selective interaction of WIPI3/4 with ATG2A/B has been elucidated by a previous structural study (*40*). In this study, we found that in addition to the

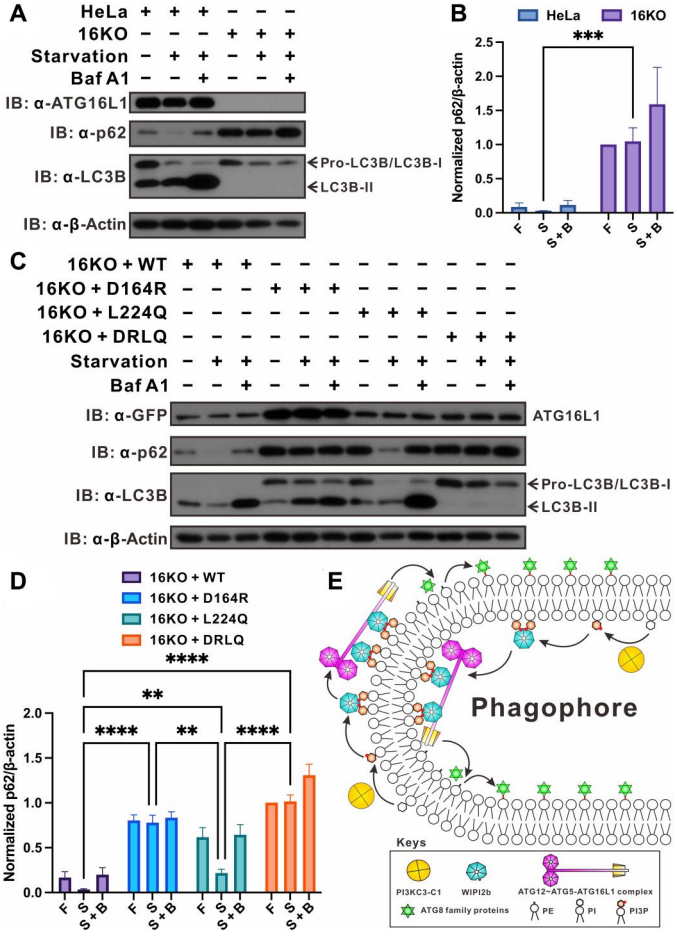

Fig. 5. Cell-based functional assays of ATG16L1 WBS1 and WBS2 in autophagy. (**A** and **C**) Western blot–based measurements of the LC3B lipidation (A) and p62 degradation (C) in HeLa cells, *ATG16L1*-knockout HeLa cells (16KO), or *ATG16L1*-knockout HeLa cells rescued with AcGFP1-tagged WT ATG16L1, AcGFP1-tagged ATG16L1 D164R mutant (D164R), AcGFP1-tagged ATG16L1 L224Q mutant (L224Q), or AcGFP1-tagged ATG16L1 D164R/L224Q mutant (DRLQ) treated for 4 hours using EBSS (starvation) or EBSS with bafilomycin A1 at 400 nM or not. Cell lysates were immunoblotted for the indicated proteins. (**B**) The levels of p62 and β-actin in (A) were quantified in ImageJ and normalized to the 16KO cells under normal condition. (**D**) The levels of p62 and β-actin in (C) were also quantified in ImageJ and normalized to the 16KO + DRLQ cells in normal condition. The data of (B) and (D) are both presented as means ± SEM from three independent experiments. Statistical analyses were both performed in GraphPad Prism 9 by two-way analysis of variance (ANOVA) followed by Bonferroni multiple comparisons test, and *P* value style is GP: $P = 0.1234$ [not significant (ns)], $^{*}P = 0.0332$, $^{**}P = 0.0021$, $^{***}P = 0.0002$, and $^{****}P < 0.0001$. (**E**) A proposed cartoon model depicting the working mode of ATG16L1 in canonical autophagy. In particular, ATG16L1 adopts a dual–binding site mode to interact with WIPI2b.

previously reported WIPI2b-binding site (WBS1), the coiled-coil region of ATG16L1 contains another functional WIPI2b-binding site (WBS2). We determined two high-resolution crystal structures of WIPI2b in complex with the WBS1 and WBS2 of ATG16L1, respectively, and uncovered the detailed binding mechanism and the key determinants for the specific association of WIPI2b with ATG16L1 (Figs. 2 and 3). Further structure-based sequence alignment analysis revealed that the key ATG16L1-binding interface residues of WIPI2b can also be found in its close homolog WIPI1 but diverge from WIPI3 and WIPI4 (fig. S21). Thus, our work may also provide a mechanistic explanation to the different autophagic functions mediated by the WIPI1/2 group and the WIPI3/4 group. Although our sequence alignment analysis showed that WIPI1 and WIPI2 share almost identical interface residues for binding to ATG16L1 (fig. S21), a previous study demonstrated that WIPI1 has a much weaker interaction with ATG16L1 compared with WIPI2b (*11*). Unfortunately, we are unable to obtain soluble WIPI1 proteins, thereby preventing detailed biochemical and structural characterizations of the interaction between WIPI1 and ATG16L1. Nevertheless, additional studies are required to elucidate the detailed mechanism governing the interaction of WIPI1 and ATG16L1 and the potential relevant regulative mechanism.

In this work, we uncovered that ATG16L1 harbors two distinct WIPI2b-binding sites, WBS1 and WBS2. On the basis of our in vitro biochemical and coimmunoprecipitation assays (Figs. 1, C to F, and 4D and figs. S3 and S17), the previously unidentified ATG16L1 WBS2 and WIPI2b interaction is much weaker and has more dynamic kinetic properties in solution compared with the ATG16L1 WBS1/WIPI2b interaction. Furthermore, our structural studies revealed that WIPI2b adopts many identical interface residues and the same pocket to interact with ATG16L1 WBS1 and WBS2 (Figs. 2 and 3). However, previous mutagenesis-based functional assays of the WIPI2b/ATG16L1 interaction from other groups were mainly conducted on WIPI2 and assessed the autophagic flux without monitoring p62 degradation in ATG16L1 WT and mutant rescue assays (*11*, *37*). Thus, the ATG16L1 WBS2/WIPI2b interaction is easy to be missed in previous studies. Our sequence alignment analysis together with relevant cell-based functional assays well demonstrated that ATG16L1 WBS2 is highly conserved even in yeast and plays crucial roles in starvation-induced autophagy (Figs. 4E and 5, A to D), in line with the fact that the ATG16L1 WBS1–disrupted mice are defective in autophagy but can still survive neonatal starvation (*41*). In the future, it will be interesting to know the potential functions of ATG16L1 WBS2/WIPI2b interaction in other autophagy processes, such as selective autophagy.

The K_d values of WBS1 and WBS2 in the ATG16L1(78 to 247) fragment for interacting with WIPI2b are 2.88 and 0.41 μM, respectively (Fig. 1D), which are smaller than the K_d values of the isolated WBS1 (3.93 μM) and WBS2 (6.88 μM) in binding to WIPI2b (Fig. 1D), indicating that there might be some cooperativities between ATG16L1 WBS1 and WBS2 in binding to WIPI2b. On the basis of our biochemical and structural analyses (Figs. 1D and 2, A to E), the WBS1 region adopts a monomeric configuration and contains many hydrophobic residues. Apparently, without any binding partners, WBS1 in the ATG16L1(78 to 247) fragment is unlikely to form a stable single-helix structure. Therefore, we speculated that the binding of WIPI2b to WBS2 may stabilize the helical structure of WBS1 to facilitate its binding for other WIPI2b molecule. On the basis of our study, the ATG16L1 WBS1 has a higher affinity than the ATG16L1 WBS2 to WIPI2b both in vitro and in vivo. Therefore, it is puzzling why the ATG16L1 WBS2 but not WBS1 is much more important for the autophagic roles of ATG16L1. Given that the yeast ATG16 only has a similar WBS2 site but not a WBS1, we speculated that the conserved ATG16L1 WBS2/WIPI2b interaction might play additional specific roles on the phagophore membrane, except for the recruitment of ATG16L1 to the phagophore. A recent study from Martens's

group (*14*) well demonstrated that ectopically targeting ATG12~ATG5-ATG16L1 complex to membranes in the absence of WIPI2 is insufficient to support the PE lipidation of ATG8 family proteins, suggesting that the WIPI2/ATG16L1 interaction on the membrane can allosterically activate the ATG12~ATG5-ATG16L1 complex. Therefore, the potential additional autophagic function endowed by the ATG16L1 WBS2/WIPI2b interaction on the phagophore membrane might explain why the ATG16L1 WBS2 but not WBS1 is much more important for the autophagic roles of ATG16L1. Nevertheless, further studies are required to elucidate the detailed underlying mechanism.

Notably, the RAB33B-binding site of ATG16L1 was proved to locate within the connecting region between ATG16L1 WBS1 and WBS2 (*23*, *24*, *42*). Our structural modeling analysis showed that RAB33B and WIPI2b can simultaneously bind to ATG16L1, but the RAB33B-binding site is very adjacent to the WIPI2b-binding WBS1 site (Fig. 4B). To reveal whether RAB33B could potentially regulate the association between WIPI2b and ATG16L1, we firstly purified the RAB33B(30 to 218) Q92L (a constitutive active RAB33B mutant) and ATG16L1(124 to 247) complex (fig. S22A). Subsequently, relevant MALS-based assays showed that the purified RAB33B(30 to 218) Q92L/ATG16L1(124 to 247) complex displays an inhomogeneous molecular weight distribution with a major species likely having a 1:2 stoichiometry in solution (fig. S22B), and the RAB33B(30 to 218) Q92L/ATG16L1(124 to 247) binary complex can further interact with WIPI2b to form a ternary complex (fig. S22C), confirming that WIPI2b and RAB33B can simultaneously bind to ATG16L1. Further quantitative ITC results showed that the binding of RAB33B to ATG16L1 has negligible effects on the ATG16L1 WBS1/WIPI2b and ATG16L1 WBS2/WIPI2b interactions (Fig. 4C; fig. S16, G and H; and table S1). Therefore, RAB33B is unlikely to regulate the interaction between WIPI2b and ATG16L1 but can work with WIPI2b to simultaneously recruit ATG16L1, in line with recent studies (*23*, *24*). It is also worthwhile to mention that three residues (I171, K179, and R193) within the coiled-coil region of ATG16L1 were demonstrated to play a critical role in the membrane targeting of ATG16L1 during starvation-induced autophagy (*43*). However, on the basis of our biochemical and structural data, the I171 residue is directly involved in the interaction with WIPI2b (Fig. 3E), and the related lipid binding–deficient ATG16L1 I171D/K179D/R193D mutation should disturb the ATG16L1 WBS2/WIPI2b binding. Meanwhile, the R193 residue of ATG16L1 was also proved to directly participate in the interaction with RAB33B (*23*), and the related ATG16L1 I171D/K179D/R193D mutation may disrupt the interaction of ATG16L1 with RAB33B. Therefore, relevant functional data from the lipid binding–deficient ATG16L1 I171D/K179D/R193D mutant should be interpreted with caution.

Phagophore membrane targeting of the E3-like ATG12~ATG5-ATG16L1 complex is a critical step for regulating the PE lipidation of ATG8 family proteins on phagophore and the subsequent autophagosome formation. To avoid unnecessary PE lipidation of ATG8 family proteins on nonautophagic membranes, the interaction of ATG16L1 with WIPI2b must be well controlled. Notably, a previous study of yeast ATG16/ATG21 interaction revealed that the stable ATG16/ATG21 complex formation preferentially occurs on membrane rather than in solution (*39*). On the basis of our structural results, the dimeric ATG16L1 can theoretically bind to four WIPI2b molecules through its WBS1 and WBS2 (Figs. 2 and 3). However, our MALS data showed that the dimeric ATG16L1(124 to 247) fragment, which contains intact WBS1 and WBS2 of ATG16L1, is unable to form a stable 2:4 stoichiometric complex with WIPI2b in solution (fig. S15), likely because of the relatively weak and dynamic ATG16L1 WBS2/WIPI2b interaction that highly resembles the yeast ATG16/ATG21 interaction. Considering that a stable 2:4 stoichiometric ATG16L1/WIPI2b complex harbors eight PI3P-binding sites, this type of weak and dynamic ATG16L1/WIPI2b interaction in solution actually should be beneficial for preventing the aberrant lipidation of ATG8 family proteins on unwanted PI3P-containing membranes in cells. However, once recruited on the phagophore membrane, owing to a high local concentration of WIPI2b and the complex membrane environment on phagophore, the dimeric ATG16L1 may simultaneously interact with four WIPI2b molecules as indicated in our structural modeling analysis (Fig. 4B). Further structural modeling analyses of the 4:2 stoichiometric WIPI2b/ATG16L1 complex with membrane showed that because the PI3P-binding FRRG motifs and the membrane-insertion regions (residues 265 to 297) of the two WIPI2b proteins bound to ATG16L1 WBS1 are located in the opposite directions, the four WIPI2b proteins bound to ATG16L1 are unlikely to simultaneously bind to PI3P and penetrate the membrane on a planar membrane (fig. S23A). However, the two WIPI2b molecules, which are located in the same side of the dimeric ATG16L1 and bind to the ATG16L1 WBS1 and WBS2 sites, respectively, can simultaneously bind to PI3P and penetrate the membrane on a planar membrane on the basis of our modeling analysis (fig. S23B). Therefore, these modeling analyses implied that the proposed 2:4 stoichiometric ATG16L1/WIPI2b complex may have a specific role at a more complex membrane interface rather than a planar membrane. Nevertheless, compared with the previously proposed single–binding site mode, the dual–binding site mode of ATG16L1/WIPI2b interaction uncovered in this study may not only provide a more efficient way to recruit ATG16L1 from cytoplasm to the WIPI2b-decorated phagophore membrane but also generate a higher avidity of the ATG16L1/WIPI2b complex on the PI3P-rich phagophore membrane.

The V231M missense mutation found in WIPI2b is closely related to a complex developmental disorder (*38*). In this study, through biochemical and structural analyses (Figs. 2F, 3F, and 4D and fig. S7B), we provided mechanistic insights into this disease-associated mutation of WIPI2b. In particular, the V231 residue of WIPI2b does not directly participate in the interaction with ATG16L1, but the V231M mutation can decrease the binding ability of WIPI2b to ATG16L1 likely through an allosteric effect. Therefore, our study also expands our understandings of the etiology of relevant diseases caused by defective WIPI2b.

Last, we proposed a model to depict the working mode of ATG16L1 in canonical autophagy (Fig. 5E). In this model, ATG16L1 associates with the ATG12~ATG5 conjugate, forming the ATG12~ATG5-ATG16L1 complex to conduct its ATG8-conjugating function (Fig. 5E). In this process, the ATG12~ATG5-ATG16L1 complex mainly functions as the downstream effector of WIPI2b that can directly sense the PI3P generated by the upstream PI3KC3-C1 complex and is specifically recruited to the nascent phagophore membrane mediated by a dual–binding site mode of ATG16L1/WIPI2b interaction as uncovered in this study. Subsequently, the recruited ATG12~ATG5-ATG16L1 complex can

act as an E3-like enzyme to facilitate the PE conjugation of ATG8 family proteins on the phagophore membrane (Fig. 5E).

MATERIALS AND METHODS

Materials

Human embryonic kidney (HEK) 293T, Platinum-E, and HeLa cell lines were provided by J. Yuan from Interdisciplinary Research Center on Biology and Chemistry, Chinese Academy of Sciences, Shanghai, China. All cell lines were cultivated with Dulbecco's modified Eagle's medium (DMEM; Thermo Fisher Scientific) supplemented with 10% fetal bovine serum (FBS; Thermo Fisher Scientific) and 1% penicillin-streptomycin (Thermo Fisher Scientific) at 37°C in humidified 5% CO_2 atmosphere. The full-length human *WIPI2b* and *ATG16L1* genes were obtained from J. Han from School of Life Sciences, Xiamen University, Xiamen, China. The full-length human *RAB33B* gene was from the cDNA library constructed from HeLa cells.

Protein expression and purification

The DNA fragment encoding WIPI2b (residues 13 to 362 without 265 to 297) were cloned into pET-SUMO-3C vector (a modified version of pET-32a vector containing an N-terminal SUMO and His_6 tag) and pRSF-Trx1-3C vector (a modified version of pRSFDuet-1 vector containing an N-terminal Thioredoxin (Trx) and His_6-tag). The DNA fragment encoding ATG16L1 (residues 207 to 247, 207 to 236, 186 to 236, 213 to 236, 221 to 236, 78 to 206, 78 to 197, 78 to 125, 124 to 197, 124 to 247, 124 to 188, and 78 to 247) were all cloned into pACYC-Trx1-3C vector (a modified version of pACYCDuet-1 vector containing an N-terminal Trx and His_6-tag). The DNA fragment encoding RAB33B (residues 30 to 218) were cloned into pRSF-SUMO1-3C vector (a modified version of pRSFDuet-1 vector containing an N-terminal SUMO and His_6-tag). For coimmunoprecipitation assays, the DNA fragments encoding human full-length ATG16L1 and WIPI2b were separately cloned into pFlag-CMV-2 vector and pEGFP-C1 vector. All point mutations of WIPI2b, ATG16L1, and RAB33B used in this study were generated through standard polymerase chain reaction–based mutagenesis method and further confirmed by DNA sequencing.

Recombinant proteins were all expressed in BL21 (DE3) *E. coli* cells induced by 200 μM isopropyl-β-D-thiogalactopyranoside at 16°C. The bacterial cell pellets were resuspended in the binding buffer (50 mM tris, 500 mM NaCl, and 5 mM imidazole at pH 7.9) and then lysed by the ultrahigh-pressure FB-110XNANO homogenizer machine (Shanghai LITU Machinery Equipment Engineering Co. Ltd.). Then, the lysis was spun down using a centrifuge at 17,000 rpm (35,000*g*) for 30 min to remove the pellet fractions. His_6-tagged proteins were purified by Ni^{2+}-NTA agarose (GE Healthcare) affinity chromatography. Each recombinant protein was further purified by size exclusion chromatography (Superdex 75 or 200 26/60 column, GE Healthcare) equilibrated with the column buffer containing 20 mM tris, 100 mM NaCl, 1 mM dithiothreitol (DTT), and 1 mM EDTA at pH 7.5. Trx-WIPI2b$^{\Delta}$ and Trx-ATG16L1(207 to 236) were coexpressed in BL21 (DE3) *E. coli* cells to obtain the WIPI2b/ATG16L1(207 to 236) complex used for crystallization. Differently, SUMO-WIPI2b$^{\Delta}$ and Trx-ATG16L1(124 to 188) were separately expressed in BL21 (DE3) *E. coli* cells and then mixed to get the WIPI2b/ATG16L1(124 to 188) complex. The N-terminal Trx or SUMO tag was cleaved by 3C protease and removed by HisTrap excel column (GE Healthcare). Last, these two complexes were further purified through Superdex 75 column equilibrated with the aforementioned column buffer.

In particular, relevant ATG16L1(124 to 247) heterodimers were generated through coexpression of myelin basic protein (MBP)–GB1–tagged ATG16L1(124 to 247) and 3xFlag-tagged ATG16L1(124 to 247) or their variants. Then, MBP and 3xFlag tags were cleaved by 3C protease and removed by HisTrap excel column (GE Healthcare), and the related ATG16L1(124 to 247) heterodimer proteins were further purified by Mono Q ion-exchange column (GE Healthcare).

Analytical gel filtration chromatography

Purified proteins were loaded on to a Superdex 200 Increase 10/300 GL or Superdex 75 10/300 GL column (GE Healthcare) equilibrated with the same column buffer. Analytical gel filtration chromatography was carried out on an AKTA FPLC system (GE Healthcare). The results were further fitted through Origin 9 software.

Multiangle light scattering

For MALS measurement, SUMO-WIPI2b$^{\Delta}$ protein, Trx-ATG16L1(207 to 247) protein, Trx-ATG16L1(78 to 206) protein, Trx-ATG16L1(78 to 247) protein, Trx-ATG16L1(78 to 197) protein, Trx-ATG16L1(78 to 125) protein, ATG16L1(124 to 247) protein, and SUMO-WIPI2b$^{\Delta}$/ATG16L1(124 to 247) complex protein samples were all injected into an AKTA FPLC system (GE Healthcare) with a Superose 200 Increase 10/300 GL or Superdex 75 10/300 GL column (GE Healthcare) with the column buffer containing 20 mM tris-HCl, 100 mM NaCl, and 1 mM DTT at pH 7.5. The chromatography system was coupled to a static light scattering detector (miniDAWN, Wyatt Technology) and a differential refractive index detector (Optilab, Wyatt Technology). Data were collected every 0.5 s with a flow rate of 0.5 ml/min. Data were analyzed using the ASTRA 6 software (Wyatt Technology) and drawn on the Origin 9 software.

ITC assay

ITC measurements were carried out on a MicroCal PEAQ-ITC (Malvern) calorimeter at 25°C. All protein samples were in the same buffer. The concentrated 50 μM proteins were loaded into the cell, and 500 μM proteins were loaded into the syringe. The titration processes were all performed by injecting proteins from syringe into the cell at time intervals of 2 min to ensure that the titration peak returned to the baseline. The titration data were analyzed using the Malvern MicroCal PEAQ-ITC analysis program and fitted using the one-site or the two-site binding mode.

Protein crystallization and structural elucidation

Crystals of the WIPI2b$^{\Delta}$/ATG16L1(207 to 236) complex and the WIPI2b$^{\Delta}$/ATG16L1(124 to 188) complex were both obtained using the sitting-drop vapor-diffusion method at 16°C. The purified WIPI2b$^{\Delta}$/ATG16L1(207 to 236) complex (20 mg/ml) was mixed with equal volumes of reservoir solution containing 30% (w/v) pentaerythritol ethoxylate (15/4 EO/OH), 100 mM MES (pH 6.5), and 50 mM magnesium chloride, while the crystal-growing condition of the WIPI2b$^{\Delta}$/ATG16L1(124 to 188) complex (24.8 mg/ml) was 0.1 M MES monohydrate (pH 6.5) and 12% (w/v) polyethylene glycol 20,000. A 1.50-Å resolution x-ray dataset for the WIPI2b$^{\Delta}$/

ATG16L1(207 to 236) complex and a 1.76-Å resolution x-ray dataset for the WIPI2b$^{\Delta}$/ATG16L1(124 to 188) complex were both collected at the beamline BL02U1, BL10U2, or BL19U1 of the Shanghai Synchrotron Radiation Facility (*44*). The diffraction data were processed upon HKL2000 (*45*) or autoPROC (*46*). The phase problems of two WIPI2b/ATG16L1 complexes were both solved by molecular replacement method using the ATG18 structure (PDB ID: 5LTG) as the search model with PHASER (*47*). The initial structural models were rebuilt manually using COOT (*48*) and then refined through PHENIX (*49*). Further manual model building and adjustments were completed via COOT (*48*). The qualities of the final models were validated by MolProbity (*50*). The final refinement statistics of solved structures in this study were listed in table S2. All the structural diagrams were prepared using the program PyMOL (www.pymol.org/).

Coimmunoprecipitation

Enhanced GFP (EGFP)–tagged WIPI2b and Flag-tagged ATG16L1 plasmids (WT or mutants) were cotransfected into HEK293T cells using Lipofectamine 2000 transfection reagent (Thermo Fisher Scientific). Cells were collected 36 hours after transfection and lysed in ice-cold cell lysis buffer (50 mM tris, 150 mM NaCl, 0.5% NP-40, 1 mM phenylmethylsulfonyl fluoride, and 1% protease inhibitor cocktail at pH 7.5) for 40 min at 4°C. Lysates were centrifuged at 14,500*g* for 15 min at 4°C to separate soluble fractions and cell debris. Supernatants were applied to anti-GFP monoclonal antibody–agarose (Medical & Biological Laboratories) and incubated for 1 hour at 4°C. The beads and nonbound proteins were separated by centrifugation at 800*g* for 3 min at 4°C. After washing three times with cold wash buffer (50 mM tris, 150 mM NaCl, and 0.1% NP-40 at pH 7.5), the beads were resuspended with the SDS-PAGE sample buffer and boiled for 5 min at 100°C. The prepared samples were analyzed by SDS-PAGE. The EGFP-tagged WIPI2b and Flag-tagged ATG16L1 were detected by Western blot using GFP antibody (1:3000 dilution; Abmart, catalog no. M20004), GFP antibody (1:4000 dilution; Proteintech, catalog no. 50430-2-AP), and Flag antibody (1:1000 dilution; Sigma-Aldrich, catalog no. F1804), respectively.

Generation of *ATG16L1*-knockout cell line

The *ATG16L1* gene was knocked out in HeLa cells using the CRISPR-Cas9 system upon a single guide RNA (sgRNA) targeting the exon 1 of *ATG16L1* gene, 5′-GCCACATCTCGGAGCAACTG-3′. The guide sequence was designed from Benchling and cloned into the LentiCRISPR v2 vector and cotransfected into HEK293T cells with pMDL and psPAX2 using Lipofectamine 2000 transfection reagent (Thermo Fisher Scientific). HeLa cells were then incubated with polybrene (Sigma-Aldrich) and virus-containing medium filtered through a 0.45-μm-pore syringe filter. Transfected HeLa cells were treated with puromycin (1.5 μg/ml; InvivoGen), and monoclonal expansion was carried out in a 96-well plate by serial dilution. Expanded single colonies were screened by Western blot using a specific ATG16L1 antibody (1:1000; Abcam, catalog no. ab187671) and further confirmed upon DNA sequencing.

Generation of relevant ATG16L1 stable cell lines

The AcGFP1-tagged WT or mutant ATG16L1 was cloned into the pMSCV-blasticidin vector and was cotransfected into Platinum-E cells with VSV.G and gag/pol using Lipofectamine 2000 transfection reagent (Thermo Fisher Scientific). Sodium butyrate (Sigma-Aldrich) was added to the culture medium at a final concentration of 5 mM. Notably, the sgRNA-targeting region of ATG16L1 at pMSCV-blasticidin vector was synonymously mutated to avoid being targeted again by Cas9 enzyme. *ATG16L1*-knockout cells were also incubated with polybrene (Sigma-Aldrich) and virus-containing medium filtered through a 0.45-μm-pore syringe filter. Transfected cells were treated with blasticidin (2 μg/ml; InvivoGen) to generate stable polyclonal cell lines.

Autophagy induction

ATG16L1-knockout HeLa cells were rescued by lentiviral transduction with AcGFP1-tagged WT ATG16L1, ATG16L1 D164R mutant (D164R), ATG16L1 L224Q mutant (L224Q), or ATG16L1 D164R/L224Q mutant (D164R/L224Q). Rescued HeLa cells were separately seeded on a six-well plate. The following day, cells were incubated for 4 hours with DMEM (Thermo Fisher Scientific) supplemented with 10% FBS (Thermo Fisher Scientific) and 1% penicillin-streptomycin (Thermo Fisher Scientific), Earle′s balanced salt solution (EBSS) (Thermo Fisher Scientific), and EBSS with bafilomycin A1 (Selleck) at 400 nM. After starvation treatment, cells were digested and resuspended with the SDS-PAGE sample buffer and boiled for 5 min at 100°C. The samples were detected by Western blot using specific ATG16L1 antibody (1:1000; Abcam, catalog no. ab187671), LC3B antibody (1:500; Abcam, catalog no. ab192890), β-actin antibody (1:5000; Proteintech, catalog no. 66009-1-lg), GFP antibody (1:1000; TaKaRa, catalog no. 632381), and p62 antibody (1:1000; Cell Signaling Technology, catalog no. #39749). The data are presented as means ± SEM from three independent experiments. Statistical analyses were performed in GraphPad Prism 9 by two-way analysis of variance (ANOVA) followed by Bonferroni multiple comparisons test, and *P* value style is GraphPad (GP): $P = 0.1234$ [not significant (ns)], $^{*}P = 0.0332$, $^{**}P = 0.0021$, $^{***}P = 0.0002$, and $^{****}P < 0.0001$.

Fluorescence imaging

Rescued HeLa cells were firstly washed with phosphate-buffered saline (PBS) and incubated respectively with DMEM (Thermo Fisher Scientific) supplemented with 10% FBS (Thermo Fisher Scientific), 1% penicillin-streptomycin (Thermo Fisher Scientific), and EBSS (Thermo Fisher Scientific). After 1.5 hours, HeLa cells were fixed with 4% paraformaldehyde for 10 min and punched with 0.2% Triton X-100 in PBS for another 10 min at room temperature, and the nuclei were visualized by staining with 4′,6-diamidino-2-phenylindole. The cell images were captured and analyzed using the TCS SP5 confocal microscope equipped with LAS X software (Leica Inc., Thornwood, NY, USA). In particular, FIP200 was stained by incubating FIP200 antibody (1:25; Proteintech, catalog no. 17250-1-AP) overnight at 4°C and goat anti-rabbit Alexa Fluor 647 (1:500; Thermo Fisher Scientific, catalog no. A28181) for 40 min at room temperature, and LC3B was then stained by incubating LC3B antibody (1:40; Cell Signaling Technology, catalog no. 83506) for 2 hours and goat anti-mouse Alexa Fluor 555 (1:500; Thermo Fisher Scientific, catalog no. A28180) for 20 min at room temperature. The statistical data represent means ± SEM of >40 analyzed cells (selected regions). Statistical analyses were performed in GraphPad Prism 9 by two-way ANOVA followed by Bonferroni multiple comparisons test and *P* value style is GP: $P = 0.1234$ (ns), $^{*}P = 0.0332$, $^{**}P = 0.0021$, $^{***}P = 0.0002$, and $^{****}P < 0.0001$.

Supplementary Materials

This PDF file includes:

Figs. S1 to S23
Tables S1 and S2

View/request a protocol for this paper from *Bio-protocol*.

REFERENCES AND NOTES

1. D. J. Klionsky, S. D. Emr, Autophagy as a regulated pathway of cellular degradation. *Science* **290**, 1717–1721 (2000).
2. B. Levine, N. Mizushima, H. W. Virgin, Autophagy in immunity and inflammation. *Nature* **469**, 323–335 (2011).
3. B. Levine, G. Kroemer, Biological functions of autophagy genes: A disease perspective. *Cell* **176**, 11–42 (2019).
4. C. A. Lamb, T. Yoshimori, S. A. Tooze, The autophagosome: Origins unknown, biogenesis complex. *Nat. Rev. Mol. Cell Biol.* **14**, 759–774 (2013).
5. N. Mizushima, T. Yoshimori, Y. Ohsumi, The role of Atg proteins in autophagosome formation. *Annu. Rev. Cell Dev. Biol.* **27**, 107–132 (2011).
6. Z. Yang, D. J. Klionsky, Eaten alive: A history of macroautophagy. *Nat. Cell Biol.* **12**, 814–822 (2010).
7. Y. C. Feng, D. He, Z. Y. Yao, D. J. Klionsky, The machinery of macroautophagy. *Cell Res.* **24**, 24–41 (2014).
8. J. H. Hurley, L. N. Young, Mechanisms of autophagy initiation. *Annu. Rev. Biochem.* **86**, 225–244 (2017).
9. C. Behrends, M. E. Sowa, S. P. Gygi, J. W. Harper, Network organization of the human autophagy system. *Nature* **466**, 68–76 (2010).
10. X. Xu, J. Liu, Y. Wang, Y. Wang, X. Gong, L. Pan, Mechanistic insights into the interactions of Ras subfamily GTPases with the SPN domain of autism-associated SHANK3. *Chinese J. Chem.* **38**, 1635–1641 (2020).
11. H. C. Dooley, M. Razi, H. E. J. Polson, S. E. Girardin, M. I. Wilson, S. A. Tooze, WIPI2 links LC3 conjugation with PI3P, autophagosome formation, and pathogen clearance by recruiting Atg12-5-16L1. *Mol. Cell* **55**, 238–252 (2014).
12. J. X. Zheng, Y. Li, Y. H. Ding, J. J. Liu, M. J. Zhang, M. Q. Dong, H. W. Wang, L. Yu, Architecture of the ATG2B-WDR45 complex and an aromatic Y/HF motif crucial for complex formation. *Autophagy* **13**, 1870–1883 (2017).
13. S. Chowdhury, C. Otomo, A. Leitner, K. Ohashi, R. Aebersold, G. C. Lander, T. Otomo, Insights into autophagosome biogenesis from structural and biochemical analyses of the ATG2A-WIPI4 complex. *Proc. Natl. Acad. Sci. U.S.A.* **115**, E9792–E9801 (2018).
14. D. Fracchiolla, C. Chang, J. H. Hurley, S. Martens, A PI3K-WIPI2 positive feedback loop allosterically activates LC3 lipidation in autophagy. *J. Cell Biol.* **219**, e201912098 (2020).
15. H. E. J. Polson, J. d. Lartigue, D. J. Rigden, M. Reedijk, S. Urbé, M. J. Clague, S. A. Tooze, Mammalian Atg18 (WIPI2) localizes to omegasome-anchored phagophores and positively regulates LC3 lipidation. *Autophagy* **6**, 506–522 (2010).
16. J. Geng, D. J. Klionsky, The Atg8 and Atg12 ubiquitin-like conjugation systems in macroautophagy. 'Protein modifications: Beyond the usual suspects' review series. *EMBO Rep.* **9**, 859–864 (2008).
17. X. Cheng, Y. Wang, Y. Gong, F. Li, Y. Guo, S. Hu, J. Liu, L. Pana, Structural basis of FYCO1 and MAP1LC3A interaction reveals a novel binding mode for Atg8-family proteins. *Autophagy* **12**, 1330–1339 (2016).
18. T. N. Nguyen, B. S. Padman, J. Usher, V. Oorschot, G. Ramm, M. Lazarou, Atg8 family LC3/GABARAP proteins are crucial for autophagosome-lysosome fusion but not autophagosome formation during PINK1/Parkin mitophagy and starvation. *J. Cell Biol.* **215**, 857–874 (2016).
19. A. Stolz, A. Ernst, I. Dikic, Cargo recognition and trafficking in selective autophagy. *Nat. Cell Biol.* **16**, 495–501 (2014).
20. C. Otomo, Z. Metlagel, G. Takaesu, T. Otomo, Structure of the human ATG12~ATG5 conjugate required for LC3 lipidation in autophagy. *Nat. Struct. Mol. Biol.* **20**, 59–66 (2013).
21. A. H. Lystad, S. R. Carlsson, L. R. de la Ballina, K. J. Kauffman, S. Nag, T. Yoshimori, T. J. Melia, A. Simonsen, Distinct functions of ATG16L1 isoforms in membrane binding and LC3B lipidation in autophagy-related processes. *Nat. Cell Biol.* **21**, 372–383 (2019).
22. Y. Fujioka, N. N. Noda, H. Nakatogawa, Y. Ohsumi, F. Inagaki, Dimeric coiled-coil structure of Saccharomyces cerevisiae Atg16 and its functional significance in autophagy. *J. Biol. Chem.* **285**, 1508–1515 (2010).
23. S. Pantoom, G. Konstantinidis, S. Voss, H. Han, O. Hofnagel, Z. Li, Y.-W. Wu, RAB33B recruits the ATG16L1 complex to the phagophore via a noncanonical RAB binding protein. *Autophagy* **17**, 2290–2304 (2021).
24. J. Metje-Sprink, J. Groffmann, P. Neumann, B. Barg-Kues, R. Ficner, K. Kühnel, A. M. Schalk, B. Binotti, Crystal structure of the Rab33B/Atg16L1 effector complex. *Sci. Rep.* **10**, 12956 (2020).
25. N. Gammoh, O. Florey, M. Overholtzer, X. J. Jiang, Interaction between FIP200 and ATG16L1 distinguishes ULK1 complex-dependent and -independent autophagy. *Nat. Struct. Mol. Biol.* **20**, 144–149 (2013).
26. T. Nishimura, T. Kaizuka, K. Cadwell, M. H. Sahani, T. Saitoh, S. Akira, H. W. Virgin, N. Mizushima, FIP200 regulates targeting of Atg16L1 to the isolation membrane. *EMBO Rep.* **14**, 284–291 (2013).
27. N. Fujita, E. Morita, T. Itoh, A. Tanaka, M. Nakaoka, Y. Osada, T. Umemoto, T. Saitoh, H. Nakatogawa, S. Kobayashi, T. Haraguchi, J. L. Guan, K. Iwai, F. Tokunaga, K. Saito, K. Ishibashi, S. Akira, M. Fukuda, T. Noda, T. Yoshimori, Recruitment of the autophagic machinery to endosomes during infection is mediated by ubiquitin. *J. Cell Biol.* **203**, 115–128 (2013).
28. M. T. Sorbara, E. G. Foerster, J. Tsalikis, M. Abdel-Nour, J. Mangiapane, I. Sirluck-Schroeder, I. Tattoli, R. van Dalen, D. E. Isenman, J. R. Rohde, S. E. Girardin, D. J. Philpott, Complement C3 drives autophagy-dependent restriction of cyto-invasive bacteria. *Cell Host Microbe* **23**, 644–652.e5 (2018).
29. B. C. King, K. Kulak, U. Krus, R. Rosberg, E. Golec, K. Wozniak, M. F. Gomez, E. Zhang, D. J. O'Connell, E. Renström, A. M. Blom, Complement component C3 is highly expressed in human pancreatic islets and prevents β cell death via ATG16L1 interaction and autophagy regulation. *Cell Metab.* **29**, 202–210.e6 (2019).
30. Y. Xu, P. Zhou, S. Cheng, Q. Lu, K. Nowak, A. K. Hopp, L. Li, X. Shi, Z. Zhou, W. Gao, D. Li, H. He, X. Liu, J. Ding, M. O. Hottiger, F. Shao, A bacterial effector reveals the V-ATPase-ATG16L1 axis that initiates xenophagy. *Cell* **178**, 552–566.e20 (2019).
31. N. Gammoh, The multifaceted functions of ATG16L1 in autophagy and related processes. *J. Cell Sci.* **133**, jcs249227 (2020).
32. N. Mizushima, A. Yamamoto, M. Hatano, Y. Kobayashi, Y. Kabeya, K. Suzuki, T. Tokuhisa, Y. Ohsumi, T. Yoshimori, Dissection of autophagosome formation using Apg5-deficient mouse embryonic stem cells. *J. Cell Biol.* **152**, 657–668 (2001).
33. L. A. Kelley, S. Mezulis, C. M. Yates, M. N. Wass, M. J. Sternberg, The Phyre2 web portal for protein modeling, prediction and analysis. *Nat. Protoc.* **10**, 845–858 (2015).
34. R. Krick, R. A. Busse, A. Scacioc, M. Stephan, A. Janshoff, M. Thumm, K. Kühnel, Structural and functional characterization of the two phosphoinositide binding sites of PROPPINs, a β-propeller protein family. *Proc. Natl. Acad. Sci. U.S.A.* **109**, E2042–E2049 (2012).
35. S. Baskaran, M. J. Ragusa, E. Boura, J. H. Hurley, Two-site recognition of phosphatidylinositol 3-phosphate by PROPPINs in autophagy. *Mol. Cell* **47**, 339–348 (2012).
36. R. Liang, J. Ren, Y. Zhang, W. Feng, Structural conservation of the two phosphoinositide-binding sites in WIPI proteins. *J. Mol. Biol.* **431**, 1494–1505 (2019).
37. L. M. Strong, C. Chang, J. F. Riley, C. A. Boecker, T. G. Flower, C. Z. Buffalo, X. Ren, A. K. H. Stavoe, E. L. F. Holzbaur, J. H. Hurley, Structural basis for membrane recruitment of ATG16L1 by WIPI2 in autophagy. *eLife* **10**, e70372 (2021).
38. M. Jelani, H. C. Dooley, A. Gubas, H. S. A. Mohamoud, M. T. M. Khan, Z. Ali, C. Kang, F. Rahim, A. Jan, N. Vadgama, M. I. Khan, J. Y. Al-Aama, A. Khan, S. A. Tooze, J. Nasir, A mutation in the major autophagy gene, WIPI2, associated with global developmental abnormalities. *Brain* **142**, 1242–1254 (2019).
39. L. Munzel, P. Neumann, F. B. Otto, R. Krick, J. Metje-Sprink, B. Kroppen, N. Karedla, J. Enderlein, M. Meinecke, R. Ficner, M. Thumm, Atg21 organizes Atg8 lipidation at the contact of the vacuole with the phagophore. *Autophagy* **17**, 1458–1478 (2021).
40. J. Ren, R. Liang, W. Wang, D. Zhang, L. Yu, W. Feng, Multi-site-mediated entwining of the linear WIR-motif around WIPI β-propellers for autophagy. *Nat. Commun.* **11**, 2702 (2020).
41. S. Rai, M. Arasteh, M. Jefferson, T. Pearson, Y. Wang, W. Zhang, B. Bicsak, D. Divekar, P. P. Powell, R. Naumann, N. Beraza, S. R. Carding, O. Florey, U. Mayer, T. Wileman, The ATG5-binding and coiled coil domains of ATG16L1 maintain autophagy and tissue homeostasis in mice independently of the WD domain required for LC3-associated phagocytosis. *Autophagy* **15**, 599–612 (2019).
42. T. Itoh, N. Fujita, E. Kanno, A. Yamamoto, T. Yoshimori, M. Fukuda, Golgi-resident small GTPase Rab33B interacts with Atg16L and modulates autophagosome formation. *Mol. Biol. Cell* **19**, 2916–2925 (2008).
43. L. J. Dudley, A. G. Cabodevilla, A. N. Makar, M. Sztacho, T. Michelberger, J. A. Marsh, D. R. Houston, S. Martens, X. Jiang, N. Gammoh, Intrinsic lipid binding activity of ATG16L1 supports efficient membrane anchoring and autophagy. *EMBO J.* **38**, e100554 (2019).
44. Z. Wang, Q. Pan, L. Yang, H. Zhou, C. Xu, F. Yu, Q. Wang, S. Huang, J. He, Automatic crystal centring procedure at the SSRF macromolecular crystallography beamline. *J. Synchrotron Radiat.* **23**, 1323–1332 (2016).
45. Z. Otwinowski, W. Minor, Processing of x-ray diffraction data collected in oscillation mode. *Methods Enzymol.* **276**, 307–326 (1997).

46. C. Vonrhein, C. Flensburg, P. Keller, A. Sharff, O. Smart, W. Paciorek, T. Womack, G. Bricogne, Data processing and analysis with the autoPROC toolbox. *Acta Crystallogr. D. Biol. Crystallogr.* **67**, 293–302 (2011).
47. L. C. Storoni, A. J. McCoy, R. J. Read, Likelihood-enhanced fast rotation functions. *Acta Crystallogr. D. Biol. Crystallogr.* **60**, 432–438 (2004).
48. P. Emsley, K. Cowtan, Coot: Model-building tools for molecular graphics. *Acta Crystallogr. D. Biol. Crystallogr.* **60**, 2126–2132 (2004).
49. P. D. Adams, R. W. Grosse-Kunstleve, L. W. Hung, T. R. Ioerger, A. J. McCoy, N. W. Moriarty, R. J. Read, J. C. Sacchettini, N. K. Sauter, T. C. Terwilliger, PHENIX: Building new software for automated crystallographic structure determination. *Acta Crystallogr. D. Biol. Crystallogr.* **58**, 1948–1954 (2002).
50. I. W. Davis, A. Leaver-Fay, V. B. Chen, J. N. Block, G. J. Kapral, X. Wang, L. W. Murray, W. B. Arendall, J. Snoeyink, J. S. Richardson, D. C. Richardson, MolProbity: All-atom contacts and structure validation for proteins and nucleic acids. *Nucleic Acids Res.* **35**, W375–W383 (2007).

Acknowledgments: We thank SSRF BL19U1, BL02U1, and BL10U2 for x-ray beam time, J. Han for the full-length WIPI2b and ATG16L1 cDNA. **Funding:** This work was supported by grants from the National Natural Science Foundation of China (92253301, 32071219, 21621002, and 21822705), the Science and Technology Commission of Shanghai Municipality (20XD1425200 and 17JC1405200), the National Basic Research Program of China (2022YFC2303102), and the Chinese Academy of Sciences (JCTD-2022-10). **Author contributions:** X.G. and L.P. designed the research. X.G., Yingli Wang, Y.T., Yaru Wang, M.Z., M.L., and Y.Z. performed the research. X.G. and L.P. analyzed the data. X.G. and L.P. wrote the paper. **Competing interests:** The authors declare that they have no competing interests. **Data and materials availability:** The coordinates and structure factors of the WIPI2b$^{\Delta}$/ATG16L1(207 to 236) complex and the WIPI2b$^{\Delta}$/ATG16L1(124 to 188) complex solved in this study have been deposited in the PDB under the accession codes 7F69 and 7XFR, respectively. All data needed to evaluate the conclusions in the paper are present in the paper and/or the Supplementary Materials.

Submitted 27 September 2022
Accepted 31 January 2023
Published 1 March 2023
10.1126/sciadv.adf0824